














Plasmonic Ferroelectric Modulator Monolithically Integrated on SiN for 216 GBd Data Transmission

M. Kohli , D. Chelladurai , A. Messner , Y. Horst , D. Moor , J. Winiger , T. Blatter , T. Buriakova, C. Convertino , F. Eltes , M. Zervas , Y. Fedoryshyn , U. Koch , and J. Leuthold , *Fellow, IEEE*

Abstract—A high-speed plasmonic barium titanate (BTO, BaTiO₃) Mach-Zehnder modulator is presented. We combine nanoscale plasmonics with BTO as solid-state active material and silicon nitride (SiN) for versatile and low loss waveguiding, and integrate them in a monolithic platform. We demonstrate a plasmonic BTO modulator processed onto foundry-produced SiN. The 15 μm long high-speed modulator features a flat electro-optic frequency response up to 70 GHz and is expected to be flat way beyond. A low $V_{\pi}L$ product of 144 Vμm is shown. Data experiments reaching 216 Gbit/s with a 216 GBd 2PAM signal and 256 Gbit/s with a 128 GBd 4PAM signal are demonstrated. The merger of the versatile silicon nitride platform with high-speed plasmonics using the highly nonlinear ferroelectric BTO is an attractive solution as a future Tb/s optical interconnect platform.

Index Terms—Barium titanate, electrooptic modulators, ferroelectric devices, high data rate, high-speed PICs, integrated photonic circuits, monolithic integration, plasmonics, silicon nitride.

I. INTRODUCTION

HIGH-SPEED integrated electro-optic modulators are vital components required for high-capacity optical links. For the employment of next generation Tb/s links to meet the exponential increase of data traffic, modulators with symbol rates beyond 100 GBd are required [1], [2], [3]. For this purpose, different physical effects are harnessed, such as the plasma dispersion effect [4], [5], [6], the quantum-confined Stark effect [7], [8], or the linear electro-optic (EO) effect, also called Pockels effect [9]. The Pockels effect is particularly interesting due to the pure phase modulation and high electro-optic bandwidth.

Manuscript received 14 December 2022; revised 10 February 2023; accepted 13 March 2023. Date of publication 30 March 2023; date of current version 27 June 2023. This work was supported by the European Commission through the Horizon 2020 projects NEBULA under Grants 871658, PlasmoniAC 871391, and NEoteRIC 871330. (Corresponding authors: M. Kohli; J. Leuthold.)

M. Kohli, D. Chelladurai, A. Messner, Y. Horst, D. Moor, J. Winiger, T. Blatter, Y. Fedoryshyn, U. Koch, and J. Leuthold are with the Institute of Electromagnetic Fields, ETH Zürich, 8092 Zürich, Switzerland (e-mail: manuel.kohli@ief.ee.ethz.ch; daniel.chelladurai@ief.ee.ethz.ch; andreas.messner@ief.ee.ethz.ch; yannik.horst@ief.ee.ethz.ch; david.moor@ief.ee.ethz.ch; joel.winiger@ief.ee.ethz.ch; tobias.blatter@ief.ee.ethz.ch; yuriy.fedoryshyn@ief.ee.ethz.ch; ueli.koch@ief.ee.ethz.ch; juerg.leuthold@ief.ee.ethz.ch).

T. Buriakova and M. Zervas are with the Ligentec SA, 1024 Ecublens, Switzerland (e-mail: tatiana.buriakova@ligentec.ch; michael.zervas@ligentec.ch).

C. Convertino and F. Eltes are with the Lumiphase AG, 8802 Kilchberg, Switzerland (e-mail: clarissa@lumiphase.com; felix@lumiphase.ch).

Color versions of one or more figures in this article are available at <https://doi.org/10.1109/JLT.2023.3260064>.

Digital Object Identifier 10.1109/JLT.2023.3260064

While modulators should be capable of high data rates, they simultaneously should feature the smallest footprints, minimal electrical energy consumption [2], [10], [11], [12], and ideally be compatible with versatile photonic platforms such as SiN for advanced applications [13], [14].

State-of-the-art integrated photonic modulators typically employ ferroelectric thin-film lithium niobate (LiNbO₃, TFLN). TFLN-based IQ modulators have already been demonstrated with bandwidth of 110 GHz and a signal rate of 130 GBd at PS-400QAM, reaching 1.96 Tbit/s net data rate with polarization multiplexing [15]. Yet, TFLN modulators typically have a large footprint with a voltage-length product of around 20 Vmm due to TFLN's relatively low Pockels coefficient of 29 pm/V [16] and the small driving electric field caused by large electrode spacing. To increase the modulation efficiency, one may utilize materials with a larger Pockels coefficient. For instance, the ferroelectric material barium titanate (BaTiO₃, BTO) offers bulk Pockels tensor elements as large as $r_{42} = 1300$ pm/V in the strained case and $r_{42} = 700$ pm/V in the strain-free case [17]. The advancement of thin-film BTO grown on silicon has already been utilized for photonic modulators [18], reaching a symbol rate of 40 GBd and a $V_{\pi}L$ of 4.5 Vmm in a BTO racetrack modulator [19]. To further decrease the footprint, the driving field strength can be increased by confining the light into a small metallic slot. This is done by the so-called plasmonic-organic-hybrid (POH) platform [20], where the metals serve simultaneously as electrodes and optical waveguides. A highly nonlinear organic material is typically used to provide the large Pockels-effect for electro-optic modulation. POH devices can be fabricated in back-end-of-the-line (BEOL) processing [21], [22], and have a small footprint, low energy consumption, and ultra-large EO bandwidth over 500 GHz [23], [24], [25]. The combination of BTO offering a large Pockels coefficient with plasmonics in order to increase the field strength has led to a plasmonic BTO modulator on silicon. Thereby, a reduction of the voltage-length product to 0.2 Vmm in a push-pull operated Mach-Zehnder modulator was shown for operation up to 72 GBd. The plasmonic BTO modulator was also found to withstand temperatures up to 250 °C [26]. BTO therefore is a solution for monolithic integration within silicon platforms [27].

While silicon is a universal platform, it faces some intrinsic challenges that come with novel applications. For instance, two-photon absorption in silicon can lead to limitations when high power is needed. This is often an issue in micro-wave photonics or all-optical processing [28]. Furthermore, the high

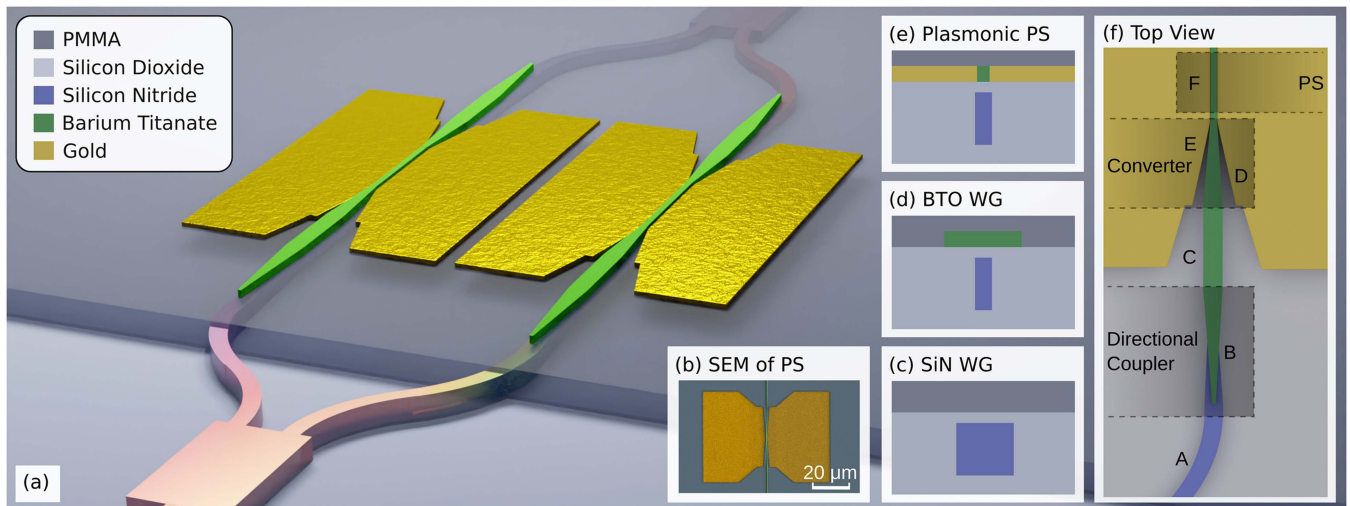


Fig. 1. Monolithic BTO plasmonic modulator on the SiN platform. (a) 3-D illustration showing the 1:2 splitting in a SiN MMI, subsequent conversion to BTO-photonic and BTO-plasmonic waveguides, and the two BTO-plasmonic phase shifters. (b) Colorized SEM image of a reference phase shifter on the same chip. (c) Cross section of the SiN waveguide embedded in SiO₂ and planarized, leaving a 100 nm thick inter-layer-oxide (ILO). (d) Cross section of the BTO access waveguide. (e) Cross-section of the plasmonic phase shifter (PS) with the metal contact next to the nano-scale slot filled with BTO. (f) Top-view of the modulator showing the directional coupler for the interlayer transition, the photonic-to-plasmonic converter and the phase shifter section. The locations A-F correspond to the electric field plots in Fig. 2.

thermo-optic coefficient induces a thermal sensitivity that hinders phase-sensitive applications. The SiN platform offers a solution to these challenges [13], [28]. SiN can handle high input power, offers a larger transparency window, a lower thermal sensitivity, relaxed fabrication tolerances because of the lower index contrast between core and cladding, and an ultra-low propagation loss [29], [30], [31], [32]. In recent years, great effort has been put into demonstrating advanced applications on the SiN platform. Among which are frequency comb generation [33], [34], Brillouin lasers [35], and on-chip amplifiers [36] to name just a few. Yet, SiN does neither have free carriers nor a second-order nonlinearity. Therefore, modulators must be integrated through other technologies. For instance, it was demonstrated that through thermally assisted electric-field poling, an effective linear EO effect can be induced up offering bandwidths in the kHz regime [37]. Examples of higher-speed modulators include the hybrid SiN approaches, where SiN is deposited on another material. For instance, with SiN deposited on TFLN, low voltage modulators [38] and data experiments up to 80 Gbit/s with a 30 GHz EO modulator [39] have been demonstrated. Other examples on the SiN platform include a graphene modulator operating at 22 Gbit/s with a 30 GHz 3 dB bandwidth [40], or a lead zirconium titanate modulator with 40 Gbit/s and a 30 GHz bandwidth [41]. Despite these advances, modulators on the SiN platform offering bandwidths that are compatible with next generation data communication links have not yet been demonstrated.

In this work, we introduce nanoscale plasmonic modulators with BTO as the active electro-optic material on the SiN platform. The modulators are monolithically integrated and combined with waveguides. For the fabrication a foundry-produced SiN platform was employed. 216 Gbit/s 2PAM and 256 Gbit/s 4PAM intensity-modulation with direct-detection (IM/DD) was shown. Bit-error-ratios (BER) were below the

soft-decision forward error correction (SD-FEC) limit. All modulation experiments were performed with a drive voltage of 1.8 V_D (3.6 V_{pp}) and a low offset bias of 3 V_{DC} to maintain poling.

The paper is organized as follows. Section II describes the device design and concept. Section III focuses on the fabrication process for the monolithic integration with the foundry-produced SiN platform. Section IV presents the characterization results, both passive and active measurements. Section V discusses the high-speed data transmission experiments. Section VI concludes the work and summarizes the key findings.

The work in this paper is in part based on our results first published at the ECOC 2022, Basel, Switzerland [42].

II. DEVICE CONCEPT AND DESIGN

A. Plasmonic Ferroelectric Modulator on SiN Platform

The plasmonic ferroelectric modulator on SiN presented in this work consists of a Mach-Zehnder modulator (MZM) interferometer configuration with one phase modulator in each arm. A schematic illustration of the devices is shown in Fig. 1(a). The MZM can be divided into three sections: the waveguide in the SiN, the interlayer transition to the BTO access waveguide, and finally the active plasmonic section.

To operate the device, light is coupled from the fiber to the SiN waveguide with efficient and fabrication-tolerant amorphous silicon (aSi) overlay grating couplers for TE polarized light [43]. The SiN is employed for passive routing and splitting with negligible losses. Fig. 1(c) depicts the cross section of the SiN waveguide embedded in SiO₂. Fig. 2(a) shows the optical mode confined to SiN. The light is split on-chip via a 1x2 multi-mode interference (MMI) coupler. The modulator has an asymmetry in the path length between the two arms of 200 μm, which allows

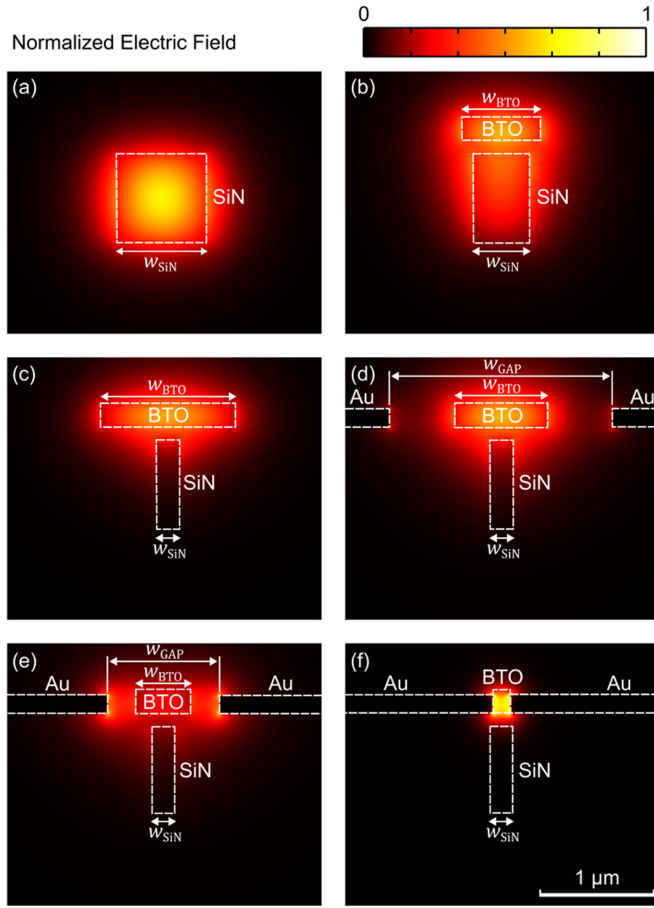


Fig. 2. Normalized electric field plots in the vertical directional coupler and photonic-to-plasmonic converter. (a)–(f) Corresponds to the location noted in Fig. 1(f) A–F. (a)–(c) Optical modes in the interlayer transition with (a) in the SiN, (b) within the directional coupler, and (c) in the BTO access waveguide. (d) and (e) tapering of the BTO and the electrode gap in the coupling section for the nano focusing, and (f) plasmonic mode with a 150 nm wide metal-insulator-metal gap filled with BTO.

wavelength tuning in addition to the controllable DC Bias for setting the operation point.

Subsequently, light is first coupled from the SiN waveguide into a BTO waveguide, and from there to an Au-BTO-Au plasmonic waveguide. Coupling from SiN to BTO is done via an 80 μm long vertical directional coupler (VDC) for the interlayer transition. The SiN waveguide reduces its size from 800 nm \times 800 nm to 200 nm \times 800 nm, whereas the BTO waveguide starts at 200 nm \times 200 nm and tapers to the nominal single-mode cross section of 1200 nm \times 200 nm, see Fig. 1(d). The normalized electric field of the mode in the SiN can be seen in Fig. 2(a) and in the BTO waveguide in Fig. 2(c), whereas (b) shows the effect of the width tapering in both, the BTO and the SiN waveguide. The SiN continues underneath the BTO and has a minimal effect on the operation. To reduce reflections at the beginning of the BTO and to enable adiabatic power transfer, both the SiN and the BTO are tapered. In Fig. 3(a), the effective index change within the VDC is plotted in red and the confinement of the electric field intensity in the BTO waveguide in yellow. At the beginning, there is no power in the BTO waveguide. The power

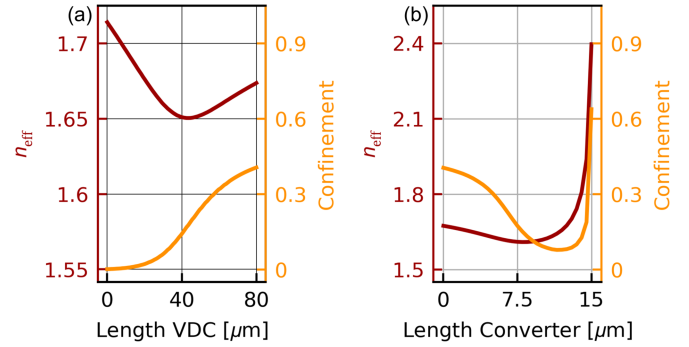


Fig. 3. Effective index and confinement in the BTO along the propagation direction for (a) the vertical directional coupler and (b) the photonic-to-plasmonic mode converter.

gradually increases to reach 0.4 in the weakly confined BTO waveguide.

The core section of the modulator is composed of the photonic-to-plasmonic converter and the plasmonic phase shifter. First, the light is coupled from the photonic BTO waveguide to the highly confined plasmonic waveguide by tapering both the BTO and the metal slot. The BTO is tapered within a length of 15 μm from 1200 nm to 150 nm width, whereas the metal starts with a separation of 3 μm and converges until it has direct contact with the BTO and forms the 150 nm wide slot. Fig. 2(c)–(f) show the modes at different locations along the propagation direction of the photonic-to-plasmonic converter. The concept of the photonic-to-plasmonic coupler can be described as a slow, quasi-adiabatic conversion from the photonic waveguide, see the normalized electric field of the mode in Fig. 2(c), to a mode as seen in Fig. 2(d) and (e). The propagation losses within the coupler increase with decreasing electrode distance, as the plasmonic contributions increase. Finally, the gold and the BTO layers converge to form the metal-insulator-metal waveguide structure. The mode conversion process is further explained in Fig. 3(b), where the effective index and confinement are plotted for the photonic-to-plasmonic converter. As both the BTO width (w_{BTO}) and the electrode gap (w_{GAP}) decreases, the light is first enhanced in the PMMA gap between the BTO and the gold, as light is pushed outside of the BTO itself. This feature behaves similarly to a hybrid-plasmonic waveguide [44]. Below a certain gap width, however, the confinement is increased with constant BTO width until the metal touches the BTO. Ideally, an adiabatic conversion between the photonic mode ($w_{GAP} \gg w_{BTO}$) and the plasmonic mode ($w_{GAP} = w_{BTO}$) should be obtained to minimize reflections and losses, potentially resulting in a very long coupler. However, because of the Ohmic losses in plasmonics, the propagation losses within the coupler must be accounted for. There are two main loss mechanisms within the coupler. First, the propagation losses throughout the coupler, and second, the mode transition when the PMMA gap vanishes. The total loss of the converter is simulated to be approximately 1 dB in a 3D FEM simulation.

B. Electro-Optic Operation Principle

The BTO plasmonic phase shifter consists of the metal-BTO-metal slot waveguide, see Fig. 4. By applying a voltage between

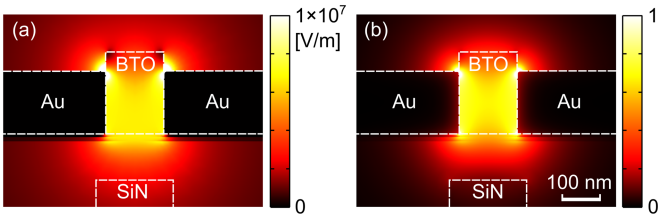


Fig. 4. (a) Normalized electric field E_{RF} within the slot when applying 1 V on one of the electrodes. (b) Optical mode E_{opt} field in the slot filled with BTO. The good overlap between the electrical and the optical modes can be seen from the two plots. The large electric and optical field strengths in the narrow slot results in efficient modulation on a small footprint.

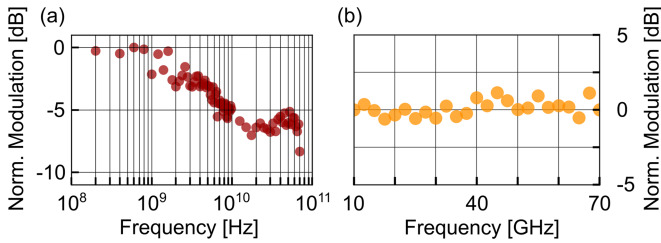


Fig. 5. (a) Normalized modulation efficiency of a reference phase shifter as a function of modulation frequency. There is an approximate drop off of 5-6 dB between the MHz and low GHz regimes. (b) Frequency response of the MZM showing a flat frequency response within 10-70 GHz.

the electrodes, the refractive index of BTO is changed by a factor determined by BTO's Pockels effect. This change is then reflected in the effective index of the propagating mode

$$\Delta n_{eff} = \Delta n_{BTO} \cdot \Gamma, \quad (1)$$

where Δn_{BTO} is the refractive index change of BTO and Γ is the field interaction factor. Simulations show that its value in the ideal structure depicted in Fig. 4 is as large as 0.96. The interaction factor depends on the cross section and the materials used. Unlike the optical confinement factor, which is defined as the fraction of light within the slot, the field interaction factor also includes the slow-down effect of plasmonics and accounts for the optical field components that overlap with the electrical field [26], [45]. The refractive index change of BTO is proportional to the electric field in the slot

$$\Delta n_{BTO} \propto r_{eff} \cdot E_{RF}, \quad (2)$$

with r_{eff} being the effective Pockels coefficient and E_{RF} the electric field in the slot. Fig. 4 shows the large overlap between (a) the electric field E_{RF} and (b) the optical mode E_{opt} , allowing for an efficient modulation on a small footprint. The simulation includes a 10 nm thick BTO slab below the electrodes in addition to the interfacial layer required for the monolithic integration of BTO.

III. FABRICATION PROCESS

The device in our work was fabricated on a combination of two platforms. For the photonic SiN platform, the waveguides were defined and cladded with oxide prior to being planarized.

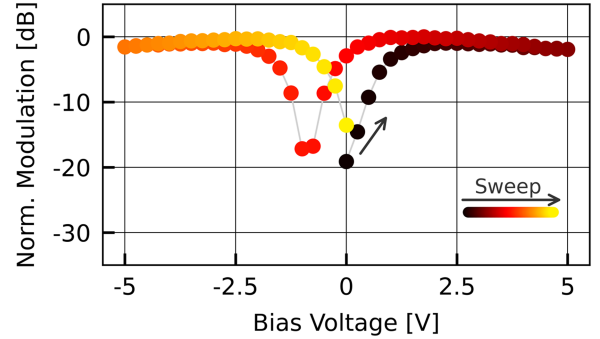


Fig. 6. (a) Normalized modulation efficiency at 40 GHz as a function of applied DC bias during operation of a reference PS on the same chip. A hysteresis can be seen when tuning forth and back. The voltage has been swept in a loop that starts and ends at 0 V.

Following the planarization, the BTO was wafer-scale integrated. The modulator itself is fabricated in a BEOL process. First, the BTO is patterned with electron beam lithography (EBL) and etched to form the waveguides and the plasmonic section. Furthermore, the amorphous silicon is deposited using plasma-enhanced chemical vapor deposition, patterned with EBL, and etched in inductively coupled reactive ion etching for the amorphous silicon overlay grating couplers. In a next step, gold is deposited to form the plasmonic modulator in addition to the photonic-to-plasmonic converter. The chip is spin-coated with polymethylmethacrylate (PMMA) as a cladding. Fig. 1(b) shows an image of the fabricated device.

IV. CHARACTERIZATION

A. Passive Optical Characterization of the MZM

In a first step, the modulator was characterized optically. A fiber-to-fiber insertion loss (IL) of below 10 dB is predicted from our simulations. This includes the negligible propagation loss in the SiN and the BTO waveguides. The vertical interlayer transition is close to lossless in simulation with < 0.1 dB. Finally, the photonic-to-plasmonic coupler has a simulated excess loss of approximately 1 dB and with the addition of plasmonic propagation losses of 0.3 dB/ μ m, the IL of the phaseshifter is expected to be 6.5 dB. Unfortunately, in this proof-of-principle fabrication, the modulator has a measured fiber-to-fiber IL of 29 dB, whereas the phase shifter (PS) itself with the plasmonic converter contributes to 20.5 dB. The coupling efficiency of the grating couplers is approximately 3.5 dB, whereas the vertical directional coupler contributes 0.75 dB per transition determined with reference devices. With the cutback measurement method, the plasmonic propagation losses are found to be 0.5 dB/ μ m and amount to 7.5 dB for the 15 μ m device. Therefore, an excess loss of 6.5 dB per photonic-to-plasmonic coupler can be identified. The main reason for the discrepancy between the measurement and simulations is the photonic-to-plasmonic converter and can be attributed to fabrication defects. By improving the metallization in the coupling section, it should be possible to decrease the IL by more than 10 dB. Further fabrication improvements

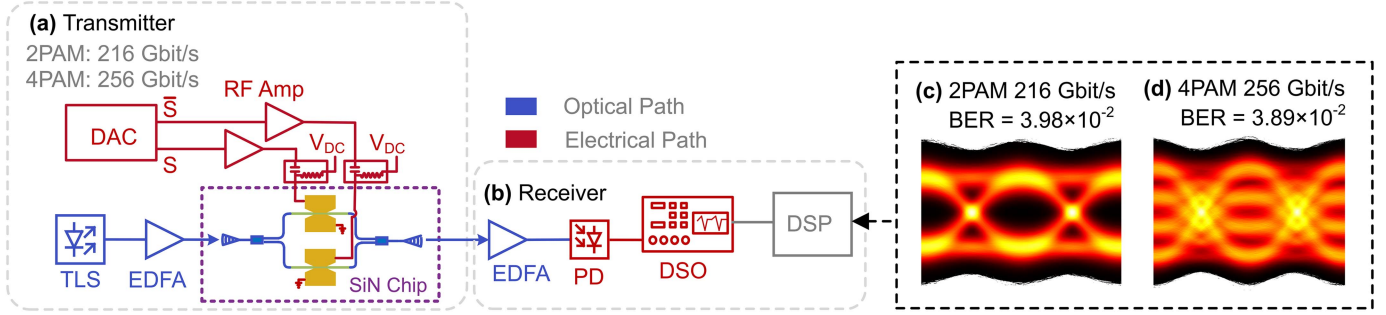


Fig. 7. (a) Schematic of the measurement setup of the transmitter and (b) of the receiver for the data transmission experiment. (c) Eye diagram of the 2PAM, 216 Gbit/s data transmission with a BER of 3.98×10^{-2} . (d) Eye diagram of the 4PAM signal transmitting at a data rate of 256 Gbit/s with a BER of 3.89×10^{-2} .

will help to reduce losses and bring them closer to the predicted values.

B. Electro-Optical Characterization

By applying a voltage to the modulator's electrodes, the resonance of the MZM is shifted due to the phase difference between the two arms and a DC half-wave voltage ($V_{\pi,DC} = 3.2$ V, $V_{\pi,DC}L = 0.048$ Vmm) was extracted. Fig. 5(a) shows the normalized modulation efficiency obtained from a reference phase shifter (PS) on the same chip in the frequency range from 100 MHz to 70 GHz. The reference PS features the same cross section and length as the MZM. A drop-off in the modulation efficiency can be observed in the range of 1-10 GHz. This drop-off potentially arises from BTO's higher electro-optical coefficient at lower frequencies and is consistent with findings in other plasmonic devices [26], [46], [47]. In Fig. 5(b), the normalized modulation efficiency of the device under test is shown. The frequency response between 10-70 GHz is comparable to the reference device and shows no dispersion across the measured range, indicating that the 3 dB bandwidth of the device itself is beyond 70 GHz. The lower frequency range was not repeated. Following the method described in [48], the high frequency half-wave voltage V_{π} can be found with

$$V_{\pi} = \frac{\pi}{4} \left(\sqrt{\frac{I(\omega_0 + 2\omega_m)}{I(\omega_0 + \omega_m)}} \right) \cdot V_m, \quad (3)$$

where V_m is the applied modulation voltage, ω_m the modulation frequency, and ω_0 the carrier frequency. The term $I(\omega_0 + \omega_m)$ denotes the intensity of the first modulation sideband and $I(\omega_0 + 2\omega_m)$ is the intensity of the second modulation sideband. The high frequency V_{π} of 9.6 V, which corresponds to a voltage-length product of only 0.144 Vmm, is larger than at DC, indicating that the MZM has a similar difference in the modulation efficiency between low frequency and the high frequency regime as found in the frequency response of Fig. 5(a). A DC bias is applied to the modulator during operation. This is needed to pole the domains of the BTO to maximize the modulation efficiency. Fig. 6 shows the normalized modulation at 40 GHz as a function of the applied DC-bias in a reference phase shifter on the same chip. The reference PS has the same cross section. The bias is swept in a loop starting at 0 V to +5 V, from +5 V

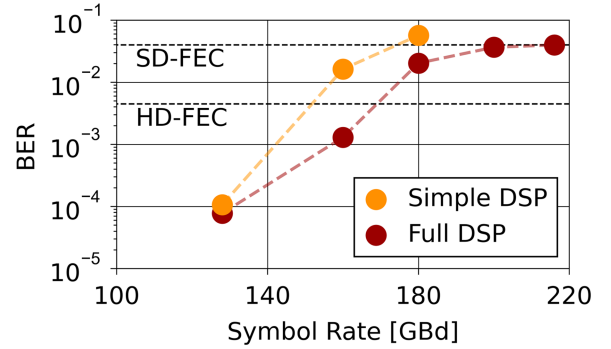


Fig. 8. BER as a function of the transmitted symbol rate with full DSP (red) and simplified DSP (yellow). DSP can be simplified to a single linear equalization stage with 151 LMS taps for 2PAM and data rates up to 160 GBd.

to -5 V, and finally from -5 V to 0 V. An expected hysteresis can be observed when sweeping back from the high voltage amplitude to the lower. The maximum modulation efficiency is achieved with a DC bias of approximately ± 2.5 V after applying the maximum bias of ± 5 V.

V. DATA EXPERIMENTS

The measurement setup of the data experiments including the eye diagrams are shown in Fig. 7. The transmitter is illustrated in Fig. 7(a) with the optical path in blue and the electrical in red. A tunable laser source (TLS) is used to generate a 1557 nm optical carrier and is amplified with an erbium doped amplifier (EDFA) to generate an 18 dBm input signal to be fed into the SiN chip. The electrical data signal was generated by a digital-to-analog converter (DAC) with a non-return-to-zero (NRZ) pulse-shape at symbol rates of up to 216 GBd. The signal comprises periodically repeated sequence lengths of minimum 2^{15} bits. The electrical analog signal was amplified to voltages of up to $1.78 V_p$ (at 128 GBd). A DC bias of only 3 V enabled by the nanoscale slot is applied for poling of the active material.

The receiver employing a direct detection scheme, see Fig. 7(b), amplifies first the signal with an EDFA. Afterwards, the signal is filtered before being fed to a photodetector (PD). After down-mixing, the electrical signal is captured with a real-time digital sampling oscilloscope (DSO) and offline digital

signal processing (DSP) is applied. For the high symbol rate experiments, the DSP consists of a timing recovery and a T/2-spaced linear equalization (LMS) with 151 taps. Furthermore, a 7-symbol pattern mapping nonlinear equalization stage and a 2nd order Volterra filter in addition to a T-spaced linear equalization with 151 taps is used. The filter taps of the linear equalizer was increased to 251 and the pattern length of the nonlinear mapping to 11 for the 2PAM 216 GBd signal.

The eye diagrams for the transmitted 216 GBd 2PAM signal are visualized in Fig. 7(c). A bit-to-error ratio (BER) of 3.98×10^{-2} was accomplished with a signal-to-noise ratio (SNR) of 6.2 dB. For the 128 GBd 4PAM signal, see Fig. 7(d), the BER was 3.89×10^{-2} with an SNR of 11.43 dB. In Fig. 8, the BER as a function of symbol rates is given. The red curve represents the received signal with full DSP described in the previous paragraph. The yellow curve, on the other hand, shows the BER for a simplified DSP, which merely consists of a clock recovery and single linear equalization stage with 151 LMS taps. The simplified DSP has a small penalty to full DSP at 128 GBd and allows for symbol rates up to 160 GBd to stay below the soft-decision FEC (SD-FEC) limit with 20 % overhead, enabled by the high-bandwidth modulator.

VI. CONCLUSION

In this work, a high-speed plasmonic ferroelectric modulator has been monolithically integrated on a foundry-produced SiN platform. We characterized the device from 100 MHz to 70 GHz and a flat frequency response above 10 GHz has been found with a voltage-length product of $144 \text{ V}\mu\text{m}$. Furthermore, we demonstrate the high-speed capabilities of this modulator with data transmission experiments reaching a symbol rate of 216 GBd in 2PAM with a BER below the SD-FEC limit and 256 Gbit/s in 4PAM modulation. Enabled by the high bandwidth of the modulator, simplified DSP can be employed for signal rates up to 160 GBd. Simulations promise a low loss (6.5 dB) modulator. This work combines the advantages of highly nonlinear and inorganic BTO with nanoscale plasmonics on the versatile and low-loss SiN employed in advanced applications for next generation Tbit/s optical links.

ACKNOWLEDGMENT

We thank the cleanroom operations team of the Binnig and Rohrer Nanotechnology Center (BRNC) for their help and support. Measurements in this study have been recorded with the free and open-source laboratory automation software “LabExT” [49].

REFERENCES

- [1] Q. Cheng, M. Bahadori, M. Glick, S. Rumley, and K. Bergman, “Recent advances in optical technologies for data centers: A review,” *Optica*, vol. 5, no. 11, pp. 1354–1370, Nov. 2018, doi: [10.1364/OPTICA.5.001354](https://doi.org/10.1364/OPTICA.5.001354).
- [2] A. Rahim et al., “Taking silicon photonics modulators to a higher performance level: State-of-the-art and a review of new technologies,” *Adv. Photon.*, vol. 3, no. 2, Apr. 2021, Art. no. 024003, doi: [10.1117/1.AP.3.2.024003](https://doi.org/10.1117/1.AP.3.2.024003).
- [3] P. J. Winzer and D. T. Neilson, “From scaling disparities to integrated parallelism: A decathlon for a decade,” *J. Lightw. Technol.*, vol. 35, no. 5, pp. 1099–1115, Mar. 2017, doi: [10.1109/JLT.2017.2662082](https://doi.org/10.1109/JLT.2017.2662082).
- [4] S. Fatholouloumi et al., “1.6 Tbps silicon photonics integrated circuit and 800 Gbps photonic engine for switch co-packaging demonstration,” *J. Lightw. Technol.*, vol. 39, no. 4, pp. 1155–1161, Feb. 2021, doi: [10.1109/JLT.2020.3039218](https://doi.org/10.1109/JLT.2020.3039218).
- [5] G. T. Reed, G. Mashanovich, F. Y. Gardes, and D. J. Thomson, “Silicon optical modulators,” *Nature Photon.*, vol. 4, no. 8, pp. 518–526, Aug. 2010, doi: [10.1038/nphoton.2010.179](https://doi.org/10.1038/nphoton.2010.179).
- [6] R. Soref and B. Bennett, “Electrooptical effects in silicon,” *IEEE J. Quantum Electron.*, vol. 23, no. 1, pp. 123–129, Jan. 1987.
- [7] D. A. B. Miller et al., “Band-edge electroabsorption in quantum well structures: The quantum-confined stark effect,” *Phys. Rev. Lett.*, vol. 53, no. 22, pp. 2173–2176, Apr. 1987, doi: [10.1103/PhysRevLett.53.2173](https://doi.org/10.1103/PhysRevLett.53.2173).
- [8] Y. Ogiso et al., “80-GHz bandwidth and 1.5-VV π InP-based IQ modulator,” *J. Lightw. Technol.*, vol. 38, no. 2, pp. 249–255, Jan. 2020, doi: [10.1109/JLT.2019.2924671](https://doi.org/10.1109/JLT.2019.2924671).
- [9] M. Thomaschewski and S. I. Bozhevolnyi, “Pockels modulation in integrated nanophotonics,” *Appl. Phys. Rev.*, vol. 9, no. 2, May 2022, Art. no. 021311, doi: [10.1063/5.0083083](https://doi.org/10.1063/5.0083083).
- [10] D. A. B. Miller, “Device requirements for optical interconnects to silicon chips,” *Proc. IEEE*, vol. 97, no. 7, pp. 1166–1185, Jul. 2009, doi: [10.1109/JPROC.2009.2014298](https://doi.org/10.1109/JPROC.2009.2014298).
- [11] D. A. B. Miller, “Attojoule optoelectronics for low-energy information processing and communications,” *J. Lightw. Technol.*, vol. 35, no. 3, pp. 346–396, Feb. 2017, doi: [10.1109/JLT.2017.2647779](https://doi.org/10.1109/JLT.2017.2647779).
- [12] Q. Xu, B. Schmidt, S. Pradhan, and M. Lipson, “Micrometre-scale silicon electro-optic modulator,” *Nature*, vol. 435, no. 7040, pp. 325–327, May 2005, doi: [10.1038/nature03569](https://doi.org/10.1038/nature03569).
- [13] Q. Wilmart et al., “A versatile silicon-silicon nitride photonics platform for enhanced functionalities and applications,” *Appl. Sci.*, vol. 9, no. 2, Jan. 2019, Art. no. 255, doi: [10.3390/app9020255](https://doi.org/10.3390/app9020255).
- [14] J. Leuthold et al., “Plasmonic data center interconnects (DCIs),” in *Proc. IEEE Opt. Fiber Commun. Conf. Exhib.*, 2021, pp. 1–3.
- [15] M. Xu et al., “Dual-polarization thin-film lithium niobate in-phase quadrature modulators for terabit-per-second transmission,” *Optica*, vol. 9, no. 1, pp. 61–62, Jan. 2022, doi: [10.1364/OPTICA.449691](https://doi.org/10.1364/OPTICA.449691).
- [16] M. Jazbinšek and M. Zgonik, “Material tensor parameters of LiNbO₃ relevant for electro-and elasto-optics,” *Appl. Phys. B*, vol. 74, no. 4, pp. 407–414, Mar. 2002, doi: [10.1007/s003400200818](https://doi.org/10.1007/s003400200818).
- [17] M. Zgonik et al., “Dielectric, elastic, piezoelectric, electro-optic, and elasto-optic tensors of BaTiO₃ crystals,” *Phys. Rev. B*, vol. 50, no. 9, pp. 5941–5949, Sep. 1994, doi: [10.1103/PhysRevB.50.5941](https://doi.org/10.1103/PhysRevB.50.5941).
- [18] C. Xiong et al., “Active silicon integrated nanophotonics: Ferroelectric BaTiO₃ devices,” *Nano Lett.*, vol. 14, no. 3, pp. 1419–1425, Jan. 2014, doi: [10.1021/nl404513p](https://doi.org/10.1021/nl404513p).
- [19] S. Abel et al., “Large Pockels effect in micro- and nanostructured barium titanate integrated on silicon,” *Nature Mater.*, vol. 18, no. 1, pp. 42–47, Jan. 2019, doi: [10.1038/s41563-018-0208-0](https://doi.org/10.1038/s41563-018-0208-0).
- [20] A. Melikyan et al., “High-speed plasmonic phase modulators,” *Nature Photon.*, vol. 8, no. 3, pp. 229–233, Feb. 2014, doi: [10.1038/nphoton.2014.9](https://doi.org/10.1038/nphoton.2014.9).
- [21] M. Ayata et al., “High-speed plasmonic modulator in a single metal layer,” *Science*, vol. 358, no. 6363, pp. 630–632, Nov. 2017, doi: [10.1126/science.aan5953](https://doi.org/10.1126/science.aan5953).
- [22] U. Koch et al., “A monolithic bipolar CMOS electronic–plasmonic high-speed transmitter,” *Nature Electron.*, vol. 3, no. 6, pp. 338–345, Jun. 2020, doi: [10.1038/s41928-020-0417-9](https://doi.org/10.1038/s41928-020-0417-9).
- [23] M. Burla et al., “500 GHz plasmonic Mach-Zehnder modulator enabling sub-THz microwave photonics,” *Amer. President Lines Photon.*, vol. 4, no. 5, May 2019, Art. no. 056106, doi: [10.1063/1.5086868](https://doi.org/10.1063/1.5086868).
- [24] C. Haffner et al., “All-plasmonic Mach-Zehnder modulator enabling optical high-speed communication at the microscale,” *Nature Photon.*, vol. 9, no. 8, pp. 525–528, Jul. 2015, doi: [10.1038/nphoton.2015.127](https://doi.org/10.1038/nphoton.2015.127).
- [25] W. Heni et al., “Plasmonic IQ modulators with attojoule per bit electrical energy consumption,” *Nature Commun.*, vol. 10, no. 1, Apr. 2019, Art. no. 1694, doi: [10.1038/s41467-019-09724-7](https://doi.org/10.1038/s41467-019-09724-7).
- [26] A. Messner et al., “Plasmonic ferroelectric modulators,” *J. Lightw. Technol.*, vol. 37, no. 2, pp. 281–290, Jan. 2019, doi: [10.1109/JLT.2018.2881332](https://doi.org/10.1109/JLT.2018.2881332).
- [27] F. Eltes et al., “A BaTiO₃-based electro-optic Pockels modulator monolithically integrated on an advanced silicon photonics platform,” *J. Lightw. Technol.*, vol. 37, no. 5, pp. 1456–1462, Mar. 2019, doi: [10.1109/JLT.2019.2893500](https://doi.org/10.1109/JLT.2019.2893500).

- [28] T. D. Bucio et al., "Silicon nitride photonics for the near-infrared," *IEEE J. Sel. Topics Quantum Electron.*, vol. 26, no. 2, pp. 1–13, Mar./Apr. 2020, doi: [10.1109/JSTQE.2019.2934127](https://doi.org/10.1109/JSTQE.2019.2934127).
- [29] R. Heideman et al., "Large-scale integrated optics using TriPleX waveguide technology: From UV to IR," in *Proc. Soc. Photographic Instrum. Eng. OPTO: Integr. Optoelectron. Devices*, 2009, pp. 203–217, doi: [10.1117/12.808409](https://doi.org/10.1117/12.808409).
- [30] C. H. Henry, R. F. Kazarinov, H. J. Lee, K. J. Orlowsky, and L. E. Katz, "Low loss Si₃N₄-SiO₂ optical waveguides on Si," *Appl. Opt.*, vol. 26, no. 13, pp. 2621–2624, Jul. 1987, doi: [10.1364/AO.26.002621](https://doi.org/10.1364/AO.26.002621).
- [31] K. Ikeda, R. E. Saperstein, N. Alic, and Y. Fainman, "Thermal and Kerr nonlinear properties of plasma-deposited silicon nitride/silicon dioxide waveguides," *Opt. Exp.*, vol. 16, no. 17, pp. 12987–12994, Aug. 2008, doi: [10.1364/OE.16.012987](https://doi.org/10.1364/OE.16.012987).
- [32] M. H. P. Pfeiffer et al., "Photonic damascene process for low-loss, high-confinement silicon nitride waveguides," *IEEE J. Sel. Topics Quantum Electron.*, vol. 24, no. 4, Jul./Aug. 2018, Art. no. 6101411, doi: [10.1109/JSTQE.2018.2808258](https://doi.org/10.1109/JSTQE.2018.2808258).
- [33] S. Kim et al., "Dispersion engineering and frequency comb generation in thin silicon nitride concentric microresonators," *Nature Commun.*, vol. 8, no. 1, Aug. 2017, Art. no. 372, doi: [10.1038/s41467-017-00491-x](https://doi.org/10.1038/s41467-017-00491-x).
- [34] A. S. Raja et al., "Electrically pumped photonic integrated soliton microcomb," *Nature Commun.*, vol. 10, no. 1, Feb. 2019, Art. no. 680, doi: [10.1038/s41467-019-08498-2](https://doi.org/10.1038/s41467-019-08498-2).
- [35] S. Gundavarapu et al., "Sub-hertz fundamental linewidth photonic integrated Brillouin laser," *Nature Photon.*, vol. 13, no. 1, pp. 60–67, Jan. 2019, doi: [10.1038/s41566-018-0313-2](https://doi.org/10.1038/s41566-018-0313-2).
- [36] Y. Liu et al., "Photonic integrated erbium-doped silicon nitride amplifiers with intense net gain," in *Proc. Conf. Lasers Electro-Opt.*, 2022, Paper SM4G.4, doi: [10.1364/CLEO_SI.2022.SM4G.4](https://doi.org/10.1364/CLEO_SI.2022.SM4G.4).
- [37] B. Zabelich, E. Nitiss, A. Stroganov, and C.-S. Brès, "Linear electro-optic effect in silicon nitride waveguides enabled by electric-field poling," *Acute Coronary Syndrome Photon.*, vol. 9, no. 10, pp. 3374–3383, Oct. 2022, doi: [10.1021/acsphotonics.2c00888](https://doi.org/10.1021/acsphotonics.2c00888).
- [38] A. N. R. Ahmed, S. Nelan, S. Shi, P. Yao, A. Mercante, and D. W. Prather, "Subvolt electro-optical modulator on thin-film lithium niobate and silicon nitride hybrid platform," *Opt. Lett.*, vol. 45, no. 5, pp. 1112–1115, Feb. 2020, doi: [10.1364/OL.381892](https://doi.org/10.1364/OL.381892).
- [39] P. Zhang et al., "High-speed electro-optic modulator based on silicon nitride loaded lithium niobate on an insulator platform," *Opt. Lett.*, vol. 46, no. 23, pp. 5986–5989, Nov. 2021, doi: [10.1364/OL.446222](https://doi.org/10.1364/OL.446222).
- [40] C. T. Phare, Y.-H. D. Lee, J. Cardenas, and M. Lipson, "Graphene electro-optic modulator with 30 GHz bandwidth," *Nature Photon.*, vol. 9, no. 8, pp. 511–514, Jul. 2015, doi: [10.1038/nphoton.2015.122](https://doi.org/10.1038/nphoton.2015.122).
- [41] K. Alexander et al., "Nanophotonic Pockels modulators on a silicon nitride platform," *Nature Commun.*, vol. 9, no. 1, Aug. 2018, Art. no. 3444, doi: [10.1038/s41467-018-05846-6](https://doi.org/10.1038/s41467-018-05846-6).
- [42] M. Kohli et al., "216 GBd plasmonic ferroelectric modulator monolithically integrated on silicon nitride," in *Proc. Eur. Conf. Opt. Commun.*, 2022, pp. 1–4.
- [43] M. Kohli et al., "Highly efficient grating coupler for silicon nitride photonics with large fabrication tolerance," in *Proc. Integr. Photon. Res. Silicon Nanophotonics*, 2021, Paper IM4A-6.
- [44] R. F. Oulton, V. J. Sorger, D. A. Genov, D. F. P. Pile, and X. Zhang, "A hybrid plasmonic waveguide for subwavelength confinement and long-range propagation," *Nature Photon.*, vol. 2, no. 8, pp. 496–500, Jul. 2008, doi: [10.1038/nphoton.2008.131](https://doi.org/10.1038/nphoton.2008.131).
- [45] J.-M. Brosi, C. Koos, L. C. Andreani, M. Waldow, J. Leuthold, and W. Freude, "High-speed low-voltage electro-optic modulator with a polymer-infiltrated silicon photonic crystal waveguide," *Opt. Exp.*, vol. 16, no. 6, pp. 4177–4191, Mar. 2008, doi: [10.1364/OE.16.004177](https://doi.org/10.1364/OE.16.004177).
- [46] D. Moor et al., ">150 GHz hybrid-plasmonic BaTiO₃-On-SOI modulator for CMOS foundry integration," in *Proc. Front. Opt. + Laser Sci.*, 2021, Paper FTh4D-2, doi: [10.1364/FIO.2021.FTh4D.2](https://doi.org/10.1364/FIO.2021.FTh4D.2).
- [47] D. Chelladurai et al., "Pockels coefficients in thin-film barium titanate and lithium niobate up to 300 GHz," in *Proc. Submitted Conf. Lasers Electro-Opt.*, 2022, Paper We5-72.
- [48] Y. Shi, L. Yan, and A. E. Willner, "High-speed electrooptic modulator characterization using optical spectrum analysis," *J. Lightw. Technol.*, vol. 21, no. 10, Oct. 2003, Art. no. 2358, doi: [10.1109/JLT.2003.818162](https://doi.org/10.1109/JLT.2003.818162).
- [49] M. Eppenberger, A. Messner, P. Wintermeyer, B. Baeuerle, and J. E. Leuthold, "LabExT — laboratory experiment tool," GitHub, 2022. [Online]. Available: <https://github.com/LabExT/LabExT>